

Random-phase Wave Splatting of Translucent Primitives for Computer-generated Holography

BRIAN CHAO*, Stanford University, USA
 JACQUELINE YANG*, Stanford University, USA
 SUYEON CHOI, Stanford University, USA
 MANU GOPAKUMAR, Stanford University, USA
 RYOTA KOISO, Stanford University, USA and KDDI Research, Japan
 GORDON WETZSTEIN, Stanford University, USA

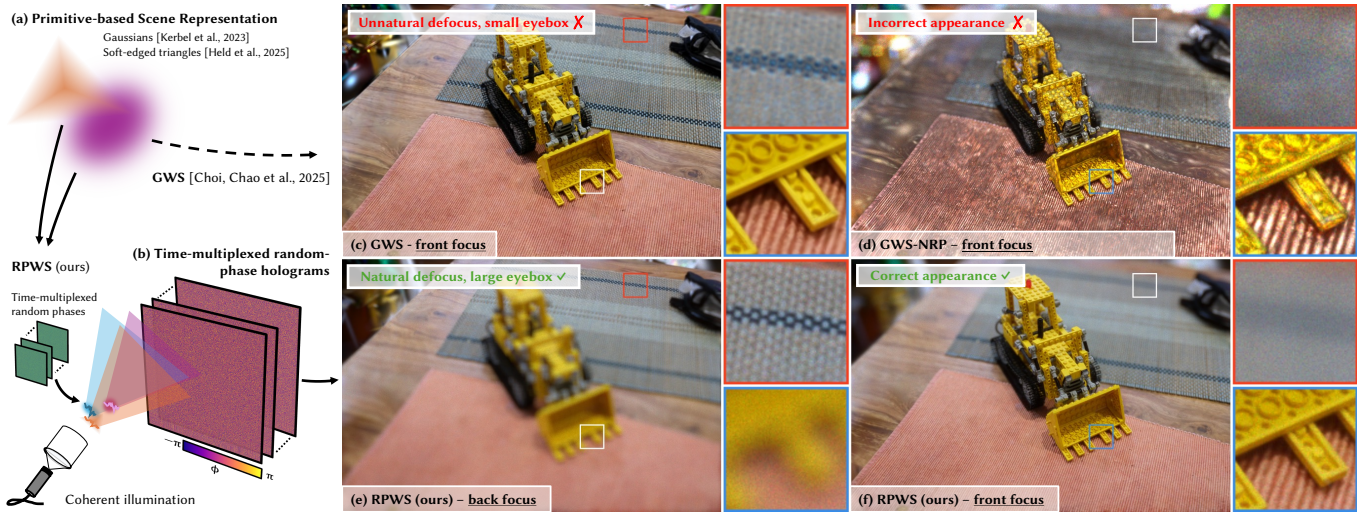


Fig. 1. Random-phase Wave Splatting (RPWS) takes in *any 2D primitive-based 3D scene representation*, including Gaussians and triangles, (a) as input and converts it into random-phase holograms (b). The prior state-of-the-art primitive-based CGH method, Gaussian Wave Splatting (GWS) [Choi et al. 2025a], is unable to accurately reconstruct natural defocus blur due to the smooth-phase nature of synthesized holograms, resulting in limited blur variation across depths and severe ringing artifacts (c). Naively applying random phase to primitives and running GWS (GWS-NRP), completely fails to reconstruct accurate appearance (d). Our RPWS algorithm, on the other hand, maximally utilizes the bandwidth of the spatial light modulator and reconstructs accurate parallax and defocus blur across the eyebox (e, f). While RPWS works for *arbitrary translucent 2D primitives*, here we show Gaussian-based wave splatting holograms for fair comparison with GWS.

Holographic near-eye displays offer ultra-compact form factors for VR/AR systems but rely on advanced computer-generated holography (CGH) algorithms to convert 3D scenes into interference patterns on spatial light modulators (SLMs). However, conventional CGH algorithms typically generate smooth-phase holograms, limiting their ability to capture view-dependent effects and realistic defocus blur while severely under-utilizing the SLM space-bandwidth product.

In this work, we propose random-phase wave splatting (RPWS), a unified wave optics rendering framework that converts *any 3D representation based on 2D translucent primitives* to random-phase holograms. Our algorithm is fully compatible with recent advances in novel 3D representations based on translucent 2D primitives, such as Gaussians and triangles, improves bandwidth utilization which effectively increases eyebox size, reconstructs

*denotes equal contribution.

Authors' Contact Information: Brian Chao, brianhc@stanford.edu, Stanford University, USA; Jacqueline Yang, jyang01@stanford.edu, Stanford University, USA; Suyeon Choi, suyeon@stanford.edu, Stanford University, USA; Manu Gopakumar, manugopa@stanford.edu, Stanford University, USA; Ryota Koiso, ryotak@stanford.edu, Stanford University, USA and KDDI Research, Japan; Gordon Wetzstein, gordon.wetzstein@stanford.edu, Stanford University, USA.

accurate defocus blur and parallax, and leverages time-multiplexed rendering not as a mere heuristic for speckle suppression, but as a mathematically exact alpha-blending mechanism derived from first principles in statistics. At the core of RPWS are (1) a fundamentally new wavefront compositing procedure and (2) an alpha-blending scheme specifically designed for arbitrary random-phase geometric primitives, ensuring physically correct color reconstruction and robust occlusion handling when compositing millions of primitives.

RPWS also departs substantially from the recent state-of-the-art primitive-based CGH algorithm, Gaussian Wave Splatting (GWS). Because GWS operates on smooth-phase primitives, it struggles to capture view-dependent effects and realistic defocus blur and severely under-utilizes the SLM space-bandwidth product; moreover, naively extending GWS to random-phase primitives fails to reconstruct accurate colors. In contrast, RPWS is designed from the ground up for arbitrary random-phase translucent primitives, and through extensive simulations and experimental validations we demonstrate that it yields state-of-the-art image quality and perceptually faithful 3D holograms for next-generation near-eye displays.

CCS Concepts: • **Computing methodologies** → **Computer graphics**; • **Hardware** → **Emerging technologies**.

Additional Key Words and Phrases: computational displays, holography, virtual reality, augmented reality, Gaussian splatting, neural rendering

1 Introduction

Holographic near-eye displays offer eyeglasses-like device form factors with unprecedented compactness for virtual and augmented reality display systems [Choi et al. 2025b; Gopakumar et al. 2024; Jang et al. 2024; Kim et al. 2022a; Maimone et al. 2017], yet require advanced computer-generated holography (CGH) algorithms to convert a target image or 3D scene into the interference pattern that can be displayed on a spatial light modulator (SLM) [Matsushima 2020; Pi et al. 2022]. Gaussian Wave Splatting (GWS) [Choi et al. 2025a] recently introduced the idea of direct hologram synthesis from Gaussian primitives [Huang et al. 2024; Kerbl et al. 2023], showing for the first time that neural scene representations can be rendered using wave optics.

However, GWS, as the name suggests, only works with Gaussian primitives, and assumes the phase distribution over the surfaces of the primitives to be near constant or *smooth*, an assumption common in the CGH literature as it typically leads to high in-focus image quality (e.g., [Maimone et al. 2017; Shi et al. 2021]). This fundamentally restricts its ability to reproduce natural defocus, parallax, and view-dependent effects. These simplifications leave a crucial gap: the holographic rendering of random-phase distributions on arbitrary primitive surfaces remains unsolved, even though it is well known that natural reflectance properties of real objects in holography can only be achieved with random phase distributions [Goodman 2015; Matsushima 2020; St-Hilaire 1995]. Neglecting these phase distributions results in an under-utilization of the inherent space-bandwidth product, or *étendue*, of an SLM, resulting in a small eyebox that leads to poor user experiences [Kim et al. 2024a, 2022b].

GWS briefly mentioned a high-level sketch in its supplementary materials on how to apply random phase to a **single Gaussian primitive** to mimic non-diffuse reflectance. However, no strategy was presented for how to **composite thousands or millions of such random-phase primitives** into a coherent hologram from standard primitive-based scene representations. A naïve extension—simply modulating each primitive wavefront with random phase and then running GWS as is (we refer to this Naïve Random-Phase extension as GWS-NRP onwards), which is suggested in the GWS supplementary materials—provably fails, as we demonstrate in Table 1, Fig. 1, Section 3.3, and throughout the paper, resulting in incorrect color reproduction as well as broken parallax and defocus. Moreover, as its name implies, GWS is restricted to Gaussian primitives. How to extend this paradigm to work with other emerging translucent primitives used for novel-view synthesis, such as soft-edged triangles [Burgdorfer and Mordohai 2025; Held et al. 2025a; Sheng et al. 2025], remains unclear. These rapid advances in neural rendering call for a generalizable CGH framework that can convert such primitives into holograms viewable on a 3D display, rather than only producing rendered 2D images.

In this work, we propose Random-phase Wave Splatting (RPWS), a unified computer-generated holography (CGH) framework that converts *3D representations based on translucent primitives*, such as Gaussians [Huang et al. 2024; Kerbl et al. 2023] and soft-edged triangles [Burgdorfer and Mordohai 2025; Held et al. 2025a; Sheng

Table 1. **Limitations of Gaussian Wave Splatting (GWS) [Choi et al. 2025a]**. GWS (1st row) generates smooth-phase holograms, resulting in unnatural defocus blur, little-to-no parallax, and small eyebox (1, 3). Naïvely applying GWS on random-phase primitives (2nd row, GWS-NRP) results in incorrect color reproduction and erroneous defocus and parallax reconstruction (2, 3). Furthermore, GWS only works with Gaussians, and it is unclear if recent advances in primitive-based representations can also benefit from this wave-splatting paradigm (4). Our random-phase wave splatting (RPWS) framework tackles all these issues.

Algorithm	1. Large eyebox	2. Correct color	3. Defocus & parallax	4. Other primitives
GWS [Choi et al. 2025a]	✗	✓	Δ	✗
GWS-NRP	✓	✗	Δ	✗
RPWS (ours)	✓	✓	✓	✓

et al. 2025], into random-phase holograms that accurately reconstruct parallax and natural defocus blur. At the core of RPWS are two key innovations: (1) a novel wave compositing procedure and (2) an intensity-domain alpha blending rule specifically designed to composite millions of random-phase primitives with continuous alpha values across their surfaces. This sharply diverges from prior silhouette-based polygon CGH methods that assume binary alpha values, and it generalizes Gaussian Wave Splatting (GWS) to support arbitrary translucent primitives. Furthermore, we prove that time-multiplexing in RPWS is not a mere heuristic for speckle reduction but the *mathematically exact mechanism* that enables physically correct alpha blending of random-phase wavefronts. These advances collectively lead to high-quality hologram synthesis from state-of-the-art primitive-based 3D scene representations, as we validate through extensive simulation and experimental results of 3D focal stacks and 4D light fields.

Specifically, our contributions include:

- Unified **wave-splatting** (Sec. 3.2) and **alpha-blending** algorithms (Sec. 3.3) that composite thousands to millions of translucent *random-phase* primitives (including Gaussians and soft-edged triangles), enabling hologram synthesis from a broad class of emerging scene representations.
- A rigorous formulation of **time multiplexing** as the exact alpha-blending mechanism for translucent wavefronts, extending far beyond prior uses as an ad-hoc speckle-reduction heuristic, and statistical optics analysis on **optimal phase distributions** for accurate random-phase alpha blending (Sec. 3.3 and supplementary materials).
- Extensive experiments, including **experimental parallax** demonstrations, showing that RPWS achieves superior image quality, perceptually correct defocus blur, and wide parallax reconstructions in both simulation and hardware (Sec. 4).

Source code and example datasets will be made public.

2 Related Work

Our work builds on a large body of research on CGH algorithms, which we review below. For a more comprehensive overview of holographic displays, we refer the reader to [Chang et al. 2020; Javidi et al. 2021; Park 2017; Pi et al. 2022; Yaraş et al. 2010].

CGH Algorithms. Holograms create a visible image or 3D scene indirectly by displaying an interference pattern, i.e., the hologram, on a 2D amplitude- or phase-only SLM. Methods that convert a target intensity distribution into a hologram are called CGH algorithms. These algorithms have been developed to accommodate a wide variety of input 3D representations, including point clouds [Chen and Wilkinson 2009a; Lucente 1993], meshes [Ahrenberg et al. 2008; Matsushima et al. 2003], wireframes [Blinder et al. 2021], light fields [Choi et al. 2022; Kang et al. 2008; Padmanaban et al. 2019; Park and Askari 2019; Zhang et al. 2019], image layers [Chen and Chu 2015; Shi et al. 2022], and most recently, Gaussians [Choi et al. 2025a]. Classic and deep learning-based *direct* CGH methods follow a common pipeline: the target intensity is first encoded into a 2D complex wavefront, typically assuming a certain phase distribution; this wavefront is then propagated to the SLM plane via models such as the angular spectrum method [Goodman 2005; Pellat-Finet 1994]; finally, the resulting complex field is converted into a phase- or amplitude-only pattern, depending on the SLM type [Maimone et al. 2017; Qi et al. 2016; Tsang and Poon 2013]. In contrast, *iterative* CGH methods make use of iterative optimization to achieve a better image quality, albeit at the cost of increased runtime [Chakravarthula et al. 2019; Fienup 1980; Gerchberg 1972; Peng et al. 2020; Zhang et al. 2017].

Phase Distributions of Holograms. Although phase is not directly observable, the phase profile of a wavefront plays a crucial role in determining the spatio-angular behavior of the observable light field [Chakravarthula et al. 2022; Kim et al. 2022b; Schiffers et al. 2023; St-Hilaire 1995]. For this reason, two popular heuristics have been developed that are widely used in CGH literature: *smooth-phase* and *random-phase* holograms [Maimone et al. 2017; Yoo et al. 2021]. Smooth-phase, sometimes called random-phase-free, holograms [Shimobaba and Ito 2015] achieve high image quality that can be demonstrated with relatively simple experimental setups [Choi et al. 2025a; Maimone et al. 2017; Peng et al. 2020; Shi et al. 2021]. The main drawback of smooth-phase distributions, however, is that they concentrate energy in the low frequencies of the angular spectrum, resulting in a severely restricted eye box size, limited defocus effects, and increased sensitivity to pupil position. These effects limit the perceptual realism and overall user experience of the produced holograms [Kim et al. 2024a] as well as the support for perceptually important focus cues [Kim et al. 2022b].

On the other hand, random-phase holograms are capable of reconstructing larger parallax and natural defocus blur, which is necessary for a perceptually realistic and natural viewing experience [Kim et al. 2024a]. However, rapid phase variations between adjacent pixels introduce unwanted speckle noise created by constructive and destructive interference [Goodman 2007]. Speckle reduction techniques often utilize some form of partial coherence, introduced by partially coherent or multiple coherent light sources, or more commonly through time multiplexing [Chao et al. 2024; Choi et al. 2022; Curtis et al. 2021; Kuo et al. 2023; Lee et al. 2020; Peng et al. 2021].

In this paper, we prove that only a specific family of random-phase distributions yields correct alpha blending of wavefronts (Sec. 3.3). We then show that the conventional uniform 2π distribution

used in prior random-phase literature conveniently happens to be one of them, allowing our RPWS holograms to maximally utilize the SLM bandwidth for large parallax and natural defocus reconstruction. Finally, we show that time multiplexing is not only a speckle reduction heuristic for random-phase holography, but the statistically exact mechanism that enables accurate alpha blending.

Primitive-based 3D Representations and CGH Algorithms.

Among the various CGH algorithms described above, polygon-based CGH algorithms that use meshes as the input 3D format are closely related to our approach [Askari et al. 2017; Chen and Wilkinson 2009b; Matsushima 2005a,b; Matsushima and Nakahara 2009; Matsushima et al. 2014; Matsushima and Sonobe 2018]. However, the constraint that each triangle has to be fully opaque limits the expressivity of mesh models by preventing soft blending of primitives, a paradigm central to recent 3D reconstruction frameworks such as 3DGS [Kerbl et al. 2023]. Coupled with per-primitive texturing, these restrictions make polygon-based CGH difficult to capture fine details without using an excessive number of tiny triangles. Gaussian Wave Splatting [Choi et al. 2025a], on the other hand, has emerged as a new primitive-based CGH algorithm that converts Gaussian-based scene representations [Huang et al. 2024; Kerbl et al. 2023] to complex holograms, greatly outperforming traditional polygon-based CGH in terms of image quality and rendering time. However, GWS does not support view-dependent effects and natural defocus due to its smooth-phase nature. Additionally, the alpha-blending and wave-splatting procedure described in GWS does not naturally extend to random-phase Gaussians. Naïvely applying GWS to random-phase wavefronts, as suggested in the GWS supplementary materials (which we refer to as GWS-NRP), provably fails as we demonstrate throughout the paper. Finally, GWS solely works with Gaussians, thus it remains unknown if such a wave compositing scheme can be extended to support a larger variety of translucent geometric primitives widely used in recent 3D reconstruction literature, such as soft-edged triangles [Burgdorfer and Mordohai 2025; Held et al. 2025a; Sheng et al. 2025].

In this work, we show that for random-phase primitive wavefronts, alpha blending is exact *in expectation* in the *intensity domain*, in contrast to the amplitude domain for smooth-phase primitives as described in GWS (Sec. 3.3). We then devise a novel wavefront composition technique that specifically works with arbitrary random-phase geometric primitives (Sec. 3.2) for accurate color reconstruction and occlusion handling. As such, our algorithm generates holograms with high image quality by fully leveraging the translucent primitive representations while synthesizing accurate defocus blur and wide parallax via random phase and time-multiplexing.

3 Wave-optics Rendering of Translucent Primitives for Computer-generated Holography

Our approach takes as input a set of multi-view images that are turned into *translucent 2D* primitives (primitives with continuous alpha values ranging from 0 to 1) representing a 3D scene. These primitives are then converted to time-multiplexed holograms through random-phase sampling. We briefly review the relevant background on emerging primitive-based scene representations (e.g. Gaussian splats [Huang et al. 2024; Kerbl et al. 2023]) and existing work

on *smooth-phase* Gaussian wave splatting, before introducing our *random-phase* wave splatting algorithm, which uniquely leverages a time-multiplexed image formation for accurate alpha blending of arbitrary geometric primitives.

3.1 Background

3.1.1 Primitive-based Scene Representations. Since the advent of 3DGS [Kerbl et al. 2023], significant research has focused on developing alternative geometric primitives for 3D scene reconstruction. Among these emerging primitive-based representations, 2D translucent primitives are notable for their local manifold structures, which enable explicit normal computation and surface extraction. Their flat-surface formulation integrates naturally with rasterization pipelines and aligns well with silhouette-based methods for polygonal CGH, allowing us to draw inspiration from prior work [Matsushima 2005a, 2020; Matsushima et al. 2014, 2003].

Examples of such 2D translucent primitives include 2D Gaussians [Huang et al. 2024] and soft-edged triangles [Burgdorfer and Mor-dohai 2025; Held et al. 2025a; Sheng et al. 2025]. For 2D Gaussians, the geometry of each of these $i = 1 \dots N$ Gaussians is described by its mean $\boldsymbol{\mu}_i \in \mathbb{R}^3$, 3D covariance $\boldsymbol{\Sigma}_i = \mathbf{R}_i \mathbf{S}_i \mathbf{S}_i^T \mathbf{R}_i^T \in \mathbb{R}^{3 \times 3}$ that can be factorized into a rotation matrix $\mathbf{R}_i \in \mathbb{R}^{3 \times 3}$ and a scaling matrix $\mathbf{S}_i \in \mathbb{R}^{3 \times 3}$. For triangles [Held et al. 2025b], the geometry of the i^{th} triangle is defined by its three vertices $\mathbf{V}_i \in \mathbb{R}^{3 \times 3}$ and a smoothness factor $\sigma_i \in \mathbb{R}$ that describes the transparency falloff from the edges of the triangle. All of these primitives typically also include two additional parameters: opacity $o_i \in \mathbb{R}$ that determines its global transparency and color $c_i \in \mathbb{R}$ (for a single color channel). Please refer to these papers for more details on the definitions of the primitives.

Any primitive-splatting approach requires the N primitives representing a scene to be depth sorted from *front to back* based on the z value with respect to the camera position, or in a holographic display setup, the SLM plane. We closely follow the *holographics* pipeline described in GWS [Choi et al. 2025a] that transforms these primitives into an adequate hologram space for CGH calculation.

3.1.2 Gaussian Wave Splatting. Gaussian Wave Splatting (GWS) [Choi et al. 2025a] is a CGH method capable of computing holograms that accurately represent 3D scenes from collections of 2D Gaussians [Huang et al. 2024] extracted from any off-the-shelf optimized 2DGS models, e.g., models optimized using the `gsp1at` library [Ye et al. 2024]. GWS first analytically determines the spectrum of each Gaussian described by its mean $\boldsymbol{\mu}_i$ and 3D covariance $\boldsymbol{\Sigma}_i$ and computes the wavefront $u_i(\mathbf{x}) = a_i(\mathbf{x})e^{ikz_i}$, where $z_i = (\boldsymbol{\mu}_i)_z$ is the Gaussian object depth and $k = \frac{2\pi}{\lambda}$. Then, each wavefront $u_i(\mathbf{x})$ is propagated using the angular spectrum propagation operator $\mathcal{P}(\cdot; z)$ [Goodman 2005; Matsushima and Shimobaba 2009] and alpha blended from *front to back* using the opacity o_i and color c_i associated with each Gaussian to get the final composited wavefront profile at the SLM, given by Eqs. 1 and 2. We refer to this process as *alpha wave blending*:

$$u_{\text{SLM}}(\mathbf{x}) = \sum_i^N \mathcal{P}\left(c_i o_i |u_i(\mathbf{x})| \mathcal{T}_i(\mathbf{x}) e^{ikz_i}; -z_i\right), \quad (1)$$

$$\mathcal{T}_i(\mathbf{x}) = \prod_{j=1}^{i-1} (1 - o_j |u_j(\mathbf{x})|). \quad (2)$$

GWS inherits the ability of Gaussian splatting to seamlessly merge large numbers of Gaussians for high-quality reconstruction. GWS further collapses classic alpha blending and volume rendering [Kajiya and Von Herzen 1984; Kerbl et al. 2023] if we ignore the wave propagation operator and match the phase of all wavefronts at all depths (i.e., $\angle u_i = kz_i$) such that the composited wavefront at the SLM plane achieves a smooth or near-constant phase profile, which we will formally derive in Section 3.3. Therefore, this formulation of GWS inherently generates “smooth-phase” holograms. Although GWS has demonstrated the potential to recreate sharp details with photorealistic image quality [Choi et al. 2025a], prior works in holography [Kim et al. 2022b; Lee et al. 2022; Schiffers et al. 2023; Shi et al. 2024] have pointed out that smooth-phase holograms are undesirable due to their poor SLM bandwidth utilization, unnatural defocus blur, large depth of field (i.e., small blur variation across different depths), and floater artifacts. GWS also requires $|u_i(\mathbf{x})|$ to be a 2D Gaussian distribution, thus its generalizability to other geometric primitives remains unknown.

Most importantly, naively extending GWS to random-phase primitives (GWS-NRP) by additionally modulating each Gaussian wavefront with a random phase map $\phi_i \stackrel{\text{iid}}{\sim} \mathcal{U}(-\pi, \pi)$ as shown below:

$$u_{\text{SLM}}(\mathbf{x}) = \sum_i^N \mathcal{P}\left(c_i o_i |u_i(\mathbf{x})| \mathcal{T}_i(\mathbf{x}) e^{ikz_i + \phi_i}; -z_i\right) \quad (3)$$

provably fails as we demonstrate in Section 3.3.

3.2 Random-phase Wave Splatting

To formally close this gap, we propose *Random-phase Wave Splatting* (RPWS), a robust CGH framework that generates random-phase holograms from translucent primitives, tackling all of the drawbacks of GWS. In RPWS, each primitive wavefront is effectively modulated by a random phase map $\phi_i(\mathbf{x})$ to scatter the light passing through each primitive in the scene away from the optical axis. The primitives are then alpha blended and composited from *back to front* with respect to the SLM, and multiple such wavefronts with individually sampled random phases are time multiplexed for accurate alpha blending to achieve the desired intensity distribution. The novel alpha blending and wave compositing procedure in RPWS is specifically designed to work with random-phase *translucent* primitives with continuous alpha values, and greatly outperforms GWS in blending complex wavefronts [Choi et al. 2025a], which we demonstrate in Sec. 4.

In Eq. 4, let $g_i(\mathbf{x})$ denote the *back-to-front* composited wavefront starting from the N^{th} primitive up to the i^{th} primitive and $M_i(\mathbf{x})$ be the transmittance mask of the i^{th} primitive. The primitive wavefront $u_i(\mathbf{x})$ denotes the wavefront generated from primitives such as Gaussians or translucent triangles (Section 4), making RPWS a plug-and-play framework for arbitrary translucent wavefronts. The

wavefront at the $i - 1^{\text{th}}$ parallel plane where the next primitive is located, which is a propagation distance $\Delta z = z_{i-1} - z_i$ away, is given by:

$$g_{i-1}^{(t)}(\mathbf{x}) = \mathcal{P}\left(M_i(\mathbf{x}) g_i(\mathbf{x}) + \sqrt{c_i} \sqrt{o_i |u_i(\mathbf{x})|} e^{i\angle u_i(\mathbf{x}) + \phi_i^{(t)}(\mathbf{x})}; \Delta z\right), \quad (4)$$

$$M_i(\mathbf{x}) = \sqrt{(1 - o_i |u_i(\mathbf{x})|)}, \quad (5)$$

where $t, 1 \leq t \leq T$ is the index of the time-multiplexed frame, T is the total number of multiplexed frames, and $\phi_i^{(t)}$ is the sampled random phase for the i^{th} primitive at the t^{th} frame. The final composited wavefront at the SLM plane that is located at $z_0 = 0$ is simply defined by $u_{\text{SLM}}^{(t)}(\mathbf{x}) = g_0^{(t)}(\mathbf{x})$. We highlight that the above procedure is highly similar to the *over* operation [Porter and Duff 1984], or Painter’s algorithm, in traditional graphics, with additional wave propagation and square root operations. This is because in RPWS, we use primitives optimized to reconstruct the *square* (i.e., intensity) of the target scene, instead of the amplitude like in GWS, which we explain in detail in the following Section 3.3.

The intensity of reconstructed images of the time-multiplexed hologram is flexibly described by the operator $\mathcal{O}(\cdot; \cdot)$ as

$$I(\mathbf{x}) = \frac{1}{T} \sum_{t=1}^T \left| \mathcal{O}\left(u_{\text{SLM}}^{(t)}(\mathbf{x}); \cdot\right) \right|^2, \quad (6)$$

where the operator $\mathcal{O}(\cdot; \cdot)$ could describe a single propagation that reconstructs a 2D image, multiple propagations that reconstruct a 3D focal stack, or the Short-time Fourier Transform (STFT) that reconstructs a 4D light field [Choi et al. 2022].

With random-phase modulation, combined with the novel wave compositing and alpha blending schemes, the bandwidth of the SLM can be maximally utilized while enabling accurate reconstruction of occlusion and color. This leads to a large eyebox and parallax, shallow depth of field (i.e., significant blur variation across depths), and natural defocus blur, as illustrated in Section 4. Please refer to the supplemental materials for a detailed statistical-optics analysis quantifying bandwidth and defocus.

3.3 Random-phase Alpha Wave Blending

RPWS departs fundamentally from GWS [Choi et al. 2025a] and prior silhouette-based methods [Matsushima et al. 2014] in its treatment of alpha blending. While earlier smooth-phase CGH approaches assumed **amplitude**-domain alpha compositing, we show that for random-phase wavefronts alpha blending is linear in the **intensity** domain *in expectation*. This crucial distinction, which is largely overlooked in prior work and GWS, directly leads to our wave compositing equation (Eq. 5), where square-root terms and time-multiplexing naturally emerge, in contrast to GWS. We analyze different alpha blending formulations in detail in Fig. 3 and in Section 4.2.2.

For simplicity, consider two primitive wavefronts at the same depth, $u_1 = \alpha_1 e^{i\phi_1}$, $u_2 = \alpha_2 e^{i\phi_2} \in \mathbb{C}^2$, with u_1 in front of u_2 . Here $\alpha_1, \alpha_2 \in \mathbb{R}^2$ are alpha maps defined as $\alpha = o \cdot \mathcal{M}$, the product of the primitive opacity $o \in \mathbb{R}$ and its transparency falloff $\mathcal{M} \in \mathbb{R}^2$ (from the Gaussian covariance/mean or the σ parameter of a translucent triangle [Held et al. 2025a]). Let $c_1, c_2 \in \mathbb{R}$ denote the scalar colors.

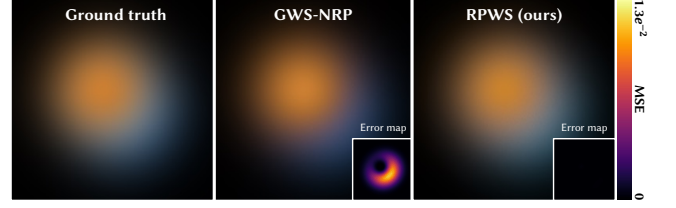


Fig. 2. **Effectiveness of RPWS sqrt-blending of random-phase wavefronts.** We show the effectiveness of our sqrt-blending procedure using the toy example described in Section 3.3 with two random-phase Gaussians, where the orange Gaussian is in front of the blue Gaussian and alpha blended. The straightforward extension of GWS amplitude-based blending with random phase (GWS-NRP) fails to reconstruct the correct appearance with significant errors near occlusion borders — which is exactly the cross term in Eq. 11. RPWS sqrt-blending achieves perfect alpha blending results.

In standard ray-based splatting [Held et al. 2025a; Huang et al. 2024; Kerbl et al. 2023], the alpha-blended color is

$$c = \alpha_1 c_1 + (1 - \alpha_1) \alpha_2 c_2, \quad (7)$$

where c is the resulting amplitude of the blended wavefront.

In wave splatting, the key question is how to alpha-blend primitive *wavefronts* in the presence of phase. Formally, this requires finding blending weights $w_1(\alpha_1, \alpha_2, c_1, c_2)$, $w_2(\alpha_1, \alpha_2, c_1, c_2) \in \mathbb{R}$ such that the amplitude of the blended wavefront

$$u = w_1(\alpha_1, \alpha_2, c_1, c_2) e^{i\phi_1} + w_2(\alpha_1, \alpha_2, c_1, c_2) e^{i\phi_2} \quad (8)$$

matches the target color c reconstructed from the input primitives.

Squaring the amplitude of both sides of Eq. 8 yields

$$c^2 = |u|^2 = |w_1 e^{i\phi_1} + w_2 e^{i\phi_2}|^2 \quad (9)$$

$$= w_1^2 + w_2^2 + w_1 w_2 \left(e^{i(\phi_1 - \phi_2)} + e^{i(\phi_2 - \phi_1)} \right) \quad (10)$$

$$= w_1^2 + w_2^2 + 2w_1 w_2 \cos(\phi_1 - \phi_2), \quad (11)$$

which shows explicit dependence on the phase distribution of $\phi_1 - \phi_2$, as analyzed below.

3.3.1 Smooth-phase (GWS): $\phi_1 - \phi_2 = 2k\pi$. When two primitive wavefronts are in phase at the same depth, $\cos(\phi_1 - \phi_2) = 1$, and Eq. 11 reduces to $(w_1 + w_2)^2$, i.e., $|u| = c = w_1 + w_2$. Comparing with Eq. 7, we set $w_1 = \alpha_1 c_1$ and $w_2 = (1 - \alpha_1) \alpha_2 c_2$, yielding

$$u = \alpha_1 c_1 e^{i\phi_1} + (1 - \alpha_1) \alpha_2 c_2 e^{i\phi_2}. \quad (12)$$

which is linear in the amplitude domain, exactly the *alpha wave blending* formulation described in GWS.

3.3.2 Random-phase (RPWS): $\phi_1, \phi_2 \stackrel{iid}{\sim} \mathcal{U}(-\pi, \pi)$. When primitives are modulated by i.i.d. random phases drawn from $\mathcal{U}(-\pi, \pi)$, the cross term $\cos(\phi_1 - \phi_2)$ in Eq. 11 is nonzero for a single realization, but only vanishes *in expectation*, which is essentially time multiplexing. Specifically, the expected intensity is

$$\mathbb{E}[|u|^2] = w_1^2 + w_2^2 + 2w_1 w_2 \mathbb{E}[\cos(\phi_1 - \phi_2)] \quad (13)$$

$$= w_1^2 + w_2^2 = c^2, \quad (14)$$

showing that cross terms are completely eliminated in the intensity domain.

To satisfy Eq. 14, we optimize primitives with the standard ray-based alpha blending rule on intensity c^2 ,

$$c^2 = \alpha'_1 c'_1 + (1 - \alpha'_1) \alpha'_2 c'_2, \quad (15)$$

and set

$$w_1 = \sqrt{\alpha'_1 c'_1}, \quad w_2 = \sqrt{(1 - \alpha'_1) \alpha'_2 c'_2}. \quad (16)$$

The resulting random-phase compositing rule is

$$u = \sqrt{\alpha'_1 c'_1} e^{i\phi_1} + \sqrt{(1 - \alpha'_1) \alpha'_2 c'_2} e^{i\phi_2}, \quad (17)$$

where each primitive wavefront is assigned color $\sqrt{c'_i}$ from a model optimized to reconstruct c^2 (intensity) rather than c (amplitude). This formulation generalizes directly to thousands or millions of random-phase primitives (Section 3.2), forming the basis of our RPWS wave-compositing algorithm in Eq. 4 and 5.

Evident from Eq. 14, we emphasize that time multiplexing is not merely an optional add-on for speckle reduction, but a fundamental requirement for correct alpha blending in our framework. The alpha blending equation is inherently stochastic: it is only satisfied in expectation over random phases, and any single realization introduces cross-term interference that corrupts the blend. Time multiplexing ensures that these cross terms vanish statistically, thereby realizing the mathematically correct alpha blending behavior in practice. In this sense, speckle reduction is only a by-product; the primary role of time multiplexing is to enforce the validity of the probabilistic alpha blending formulation itself. We further derive exact convergence bounds in the supplemental materials, showing that the uniform 2π phase distribution belongs to a class of phase distributions that achieve the optimal $O(1/\sqrt{N})$ decay of cross terms, thereby providing formal justification for our probabilistic alpha blending framework.

3.4 Applying Random Phase to Primitives

To apply random phase to primitive surfaces, we adopt the heuristic briefly mentioned in the supplementary materials of GWS [Choi et al. 2025a]. While GWS only alluded to this idea qualitatively, we provide, **for the first time**, a rigorous mathematical formulation grounded in statistical optics that proves this heuristic to be exact, and demonstrate its practical applications such as programmatic depth-of-field control. Please refer to the supplementary materials of this paper for more details.

4 Experiments

4.1 Implementation Details

We generate 3D holograms of scenes from the Blender [Mildenhall et al. 2020] and MipNeRF-360 [Barron et al. 2022] datasets using 2D Gaussians, textured meshes, and translucent triangles. Following GWS [Choi et al. 2025a], we prepare 3D scene representations with the open-source `gsplat` library [Ye et al. 2024] for 2DGS, NeRF2Mesh models [Tang et al. 2023] for textured meshes, and Triangle Splatting models [Held et al. 2025a] for translucent triangles. Additional data preparation details are provided in the supplemental materials.

We implement our algorithms in PyTorch and build a benchtop holographic display for experimental validation. Please refer to the

CGH Algorithm	Blender	Mip-NeRF 360
Polygons-RP (1 frame) [Matsushima 2005a]	17.02 / 0.14 / 0.75	12.77 / 0.14 / 0.76
Polygons-RP (8 frames) [Matsushima 2005a]	20.27 / 0.30 / 0.65	15.63 / 0.27 / 0.69
RPWS-GS (1 frame)	18.11 / 0.15 / 0.76	14.17 / 0.17 / 0.76
RPWS-GS (8 frames)	23.42 / 0.36 / 0.64	19.65 / 0.36 / 0.65
RPWS-GS (24 frames)	24.87 / 0.49 / 0.56	21.21 / 0.48 / 0.58
GWS [Choi et al. 2025a]	14.35 / 0.18 / 0.63	10.50 / 0.17 / 0.60

Table 2. **Quantitative light-field reconstruction performance of different CGH algorithms.** We evaluate the image quality of 10×10 dense light fields reconstructed from the simulated holograms generated using different CGH methods in terms of PSNR (\uparrow) / SSIM (\uparrow) / LPIPS (\downarrow). The best performing metrics for all CGH baselines are boldfaced. Our method achieves the best image light-field reconstruction performance and eyebox uniformity among all CGH baselines.

supplementary materials for detailed pseudocode and hardware specifications.

4.2 Simulation and Experimental Results

4.2.1 Baseline Comparisons with Simulation Results. We compare RPWS against several primitive-based CGH baselines, including random-phase polygon-based CGH (Polygons-RP) via the silhouette method [Matsushima 2005b; Matsushima and Nakahara 2009; Matsushima et al. 2003] and its time-multiplexed variants (1 and 8 frames), as well as Gaussian Wave Splatting (GWS) [Choi et al. 2025a]. For all quantitative and qualitative baseline comparisons, we restrict RPWS to 2DGS representations (RPWS-GS), where the number of Gaussians can be matched directly to the number of polygon primitives (using 3DGS-MCMC [Kheradmand et al. 2024]) for fair comparisons, similar to GWS. For RPWS with soft-edged triangle primitives [Burgdorfer and Mordohai 2025; Held et al. 2025a; Sheng et al. 2025], which we denote as RPWS- Δ , we pick triangle splatting [Held et al. 2025a] as the representative method. Since triangle splatting does not allow for exact primitive count control, we only show qualitative results of RPWS- Δ .

Fig. 4-(a) and 5-(a) compare simulated focal stacks of the synthesized holograms. GWS produces smooth-phase holograms with little depth-dependent variation, yielding unnatural coherent blur with ringing artifacts. Single-frame random-phase holograms (Polygon-RP, RPWS) exhibit strong speckle, but quality improves with time multiplexing (8, 24 frames). Polygon-RP produces more natural defocus blur, but its in-focus fidelity is limited by the low-quality per-face textured mesh representation. Both RPWS-GS and RPWS- Δ achieves the most natural defocus blur, closely matching incoherent blur, while maintaining in-focus quality comparable to GWS.

Fig. 4-(b) and 5-(b) compare simulated light fields of the synthesized holograms using individual views and epipolar images. For smooth-phase GWS, wavefront energy concentrates near the eyebox center, causing severe degradation at the periphery. In contrast, RPWS-GS and RPWS- Δ distribute energy evenly across the eyebox, enabling accurate view reconstruction at all pupil positions. Random-phase polygon-based CGH again suffers from the coarse per-face textured mesh representation. Quantitative results

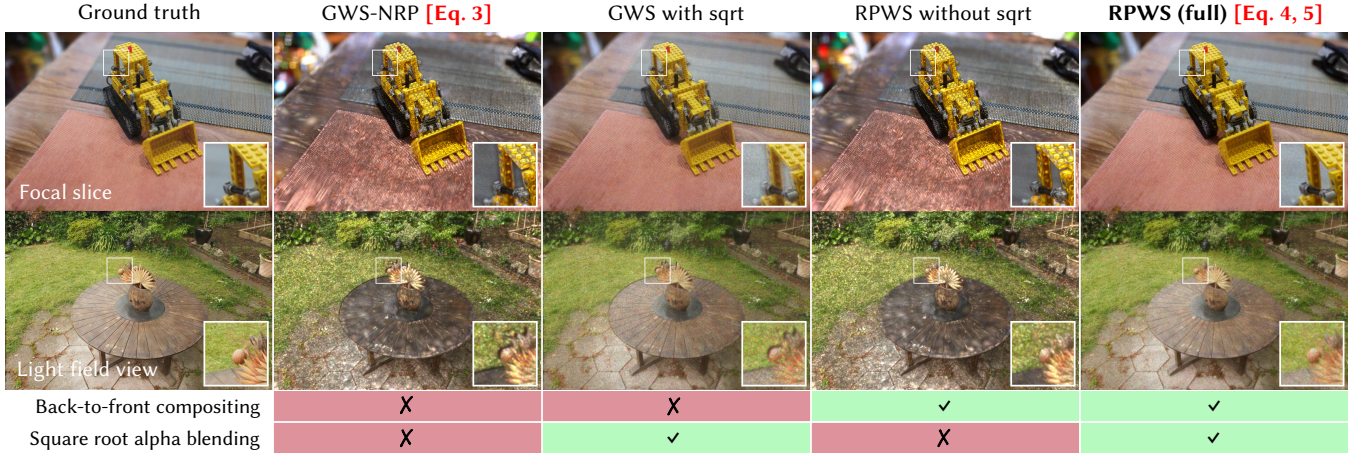


Fig. 3. **Ablation study on random-phase CGH rendering algorithms.** We compare our RPWS algorithm with three other alpha blending methods on random-phase primitives. (a) Naïvely applying random phase to GWS fails to reconstruct accurate appearance. (b) GWS with our square root alpha blending formulation generates somewhat accurate appearance. However, incorrect occlusion handling at depth discontinuities manifests as light leakage and halo artifacts in focal stacks and black holes near occlusion borders. This is an artifact frequently observed in conventional multifocal displays [Chang et al. 2020; Mercier et al. 2017; Narain et al. 2015]. (c) RPWS without square root-based blending also fails to reconstruct accurate colors. (d) Our full RPWS model reconstructs accurate color, natural defocus blur, and physically-correct parallax. Please refer to the supplementary materials for equations and pseudocodes of all alpha-blending formulations.

for dense 10×10 light-field reconstructions, measured with standard image quality metrics, are reported in Table 2 where RPWS clearly outperforms all methods.

Despite belonging to fundamentally different algorithmic classes, we delineate the key distinctions between RPWS and STFT-based light field CGH methods [Choi et al. 2022; Kim et al. 2024b] and perform additional baseline comparisons in the supplementary materials.

4.2.2 Experimentally Captured Focal Stack and Parallax Results.

We experimentally capture reconstructed focal stacks and *light fields* of RPWS and other CGH baselines to demonstrate real-world refocusing capabilities and parallax effects. Individual frames and color channels are captured independently and merged in post-processing. The experimentally captured results well match the simulation results, as shown in Fig. 6. Our method (both RPWS-GS and RPWS- Δ) achieves the best balance between high in-focus image quality and natural defocus blur, while correctly reconstructing parallax.

4.2.3 Ablation Study on Alpha-Blending Operations. To our knowledge, no effective method was ever presented to alpha-blend *complex, translucent wavefronts*. We thus extend GWS [Choi et al. 2025a] to support random-phase alpha blending by simply modulating each Gaussian with random phase and running GWS as is, and ablate the wave splatting and intensity-based alpha blending designs in Fig. 3. Naïvely adding random phase to GWS (GWS-NRP) fails to reconstruct accurate appearance. With square root alpha blending, GWS yields somewhat plausible results. However, the resulting focal stacks exhibit prominent dark halo and light leakage artifacts at depth discontinuities. In light field reconstruction, this manifests as dark borders around foreground occluders.

Our final RPWS algorithm, which combines the square root alpha-blending formulation *and* the back-to-front wave compositing procedure, achieves the most accurate focal stack reconstruction and parallax rendering results, completely eliminating artifacts at depth discontinuities and occlusion borders while accurately reconstructing image content. Please refer to the supplemental materials for intuitive visual illustrations and explanations of each alpha blending method and why all fail except for ours.

5 Discussion

Limitations and Future Work. In RPWS, time multiplexing is used to realize mathematically exact alpha blending, hence many frames are required for accurate reconstruction. In practice, the effectiveness of time multiplexing is constrained by SLM refresh rates, though this limitation may be alleviated by advances in high-speed SLMs, such as the 3600 fps FLCoS used in Holographic Parallax [Kim et al. 2024a] and the recently developed 5760 fps TI MEMS-based PLM. Addressing quantization artifacts in these devices presents an interesting future direction. Our experiments also show reduced contrast due to random phase, but extending learning-based calibration techniques [Choi et al. 2022; Peng et al. 2020] to directly reconstruct random-phase complex fields [Jang et al. 2024] may further enhance RPWS holograms. Please refer to the supplemental materials for more discussions on contrast enhancement strategies.

Conclusion. Random-phase Wave Splatting enables photorealistic CGH with correct defocus blur and parallax, unlocking perceptually realistic VR. It generalizes beyond Gaussians to diverse translucent primitives, seamlessly bridging modern neural scene representations with next-generation display technology.

References

- Lukas Ahrenberg, Philip Benzie, Marcus Magnor, and John Watson. 2008. Computer generated holograms from three dimensional meshes using an analytic light transport model. *Applied optics* 47, 10 (2008), 1567–1574.
- Mehdi Askari, Seong-Bok Kim, Kwang-Soo Shin, Seok-Bum Ko, Sang-Hoo Kim, Dae-Youl Park, Yeon-Gyeong Ju, and Jae-Hyeung Park. 2017. Occlusion handling using angular spectrum convolution in fully analytical mesh based computer generated hologram. *Optics Express* 25, 21 (2017), 25867–25878.
- Jonathan T. Barron, Ben Mildenhall, Dor Verbin, Pratul P. Srinivasan, and Peter Hedman. 2022. Mip-NeRF 360: Unbounded Anti-Aliased Neural Radiance Fields. In *CVPR*.
- David Blinder, Takashi Nishitsuji, and Peter Schelkens. 2021. Real-time computation of 3D wireframes in computer-generated holography. *IEEE Transactions on Image Processing* 30 (2021), 9418–9428.
- Nathaniel Burgdorfer and Philippos Mordohai. 2025. Radiant Triangle Soup with Soft Connectivity Forces for 3D Reconstruction and Novel View Synthesis. arXiv:2505.23642 [cs.CV] <https://arxiv.org/abs/2505.23642>
- Praneeth Chakravarthula, Seung-Hwan Baek, Florian Schiffers, Ethan Tseng, Grace Kuo, Andrew Maimone, Nathan Matsuda, Oliver Cossairt, Douglas Lanman, and Felix Heide. 2022. Pupil-aware Holography. *ACM Transactions on Graphics (TOG)* 41, 6, Article 212 (2022).
- Praneeth Chakravarthula, Yifan Peng, Joel Kollin, Henry Fuchs, and Felix Heide. 2019. Wirtinger holography for near-eye displays. *ACM Transactions on Graphics (TOG)* 38, 6 (2019), 1–13.
- Chenliang Chang, Kiseung Bang, Gordon Wetzstein, Byoungcho Lee, and Liang Gao. 2020. Toward the next-generation VR/AR optics: a review of holographic near-eye displays from a human-centric perspective. *Optica* 7, 11 (2020), 1563–1578.
- Brian Chao, Manu Gopakumar, Suyeon Choi, Jonghyun Kim, Liang Shi, and Gordon Wetzstein. 2024. Large Étendue 3D Holographic Display with Content-adaptive Dynamic Fourier Modulation. In *SIGGRAPH Asia 2024 Conference Papers*. 1–12.
- J-S Chen and DP Chu. 2015. Improved layer-based method for rapid hologram generation and real-time interactive holographic display applications. *Optics express* 23, 14 (2015), 18143–18155.
- Rick H.-Y. Chen and Timothy D Wilkinson. 2009a. Computer generated hologram from point cloud using graphics processor. *Applied optics* 48, 36 (2009), 6841–6850.
- Rick H-Y Chen and Timothy D Wilkinson. 2009b. Computer generated hologram with geometric occlusion using GPU-accelerated depth buffer rasterization for three-dimensional display. *Applied optics* 48, 21 (2009), 4246–4255.
- Suyeon Choi, Brian Chao, Jacqueline Yang, Manu Gopakumar, and Gordon Wetzstein. 2025a. Gaussian Wave Splatting for Computer Generated Holography. *ACM Transactions on Graphics (TOG)* 44, 4 (2025), 1–11.
- Suyeon Choi, Manu Gopakumar, Yifan Peng, Jonghyun Kim, Matthew O’Toole, and Gordon Wetzstein. 2022. Time-multiplexed neural holography: a flexible framework for holographic near-eye displays with fast heavily-quantized spatial light modulators. In *ACM SIGGRAPH 2022 Conference Proceedings*. 1–9.
- Suyeon Choi, Changwon Jang, Douglas Lanman, and Gordon Wetzstein. 2025b. Synthetic aperture waveguide holography for compact mixed reality displays with large étendue. *Nature Photonics* (2025).
- Vincent R Curtis, Nicholas W Caira, Jiayi Xu, Asha Gowda Sata, and Nicolas C Pégard. 2021. DCGH: dynamic computer generated holography for speckle-free, high fidelity 3D displays. In *2021 IEEE Virtual Reality and 3D User Interfaces (VR)*. IEEE, 1–9.
- JR Fienup. 1980. Iterative method applied to image reconstruction and to computer-generated holograms. *Optical Engineering* 19, 3 (1980), 297–305.
- Ralph W Gerchberg. 1972. A practical algorithm for the determination of plane from image and diffraction pictures. *Optik* 35, 2 (1972), 237–246.
- Joseph W Goodman. 2005. *Introduction to Fourier optics*. Roberts and Company publishers.
- Joseph W Goodman. 2007. *Speckle phenomena in optics: theory and applications*. Roberts and Company Publishers.
- Joseph W. Goodman. 2015. *Statistical Optics* (2nd ed.). Wiley.
- Manu Gopakumar, Gun-Yeal Lee, Suyeon Choi, Brian Chao, Yifan Peng, Jonghyun Kim, and Gordon Wetzstein. 2024. Full-colour 3D holographic augmented-reality displays with metasurface waveguides. *Nature* (2024), 1–7.
- Jan Held, Renaud Vandeghen, Adrien Deliege, Abdullah Hamdi, Anthony Cioppa, Silvio Giancola, Andrea Vedaldi, Bernard Ghanem, Andrea Tagliasacchi, and Marc Van Droogenbroeck. 2025a. Triangle Splatting for Real-Time Radiance Field Rendering. *arXiv* (2025).
- Jan Held, Renaud Vandeghen, Abdullah Hamdi, Adrien Deliege, Anthony Cioppa, Silvio Giancola, Andrea Vedaldi, Bernard Ghanem, and Marc Van Droogenbroeck. 2025b. 3D Convex Splatting: Radiance Field Rendering with 3D Smooth Convexes. In *Proceedings of the IEEE/CVF Conference on Computer Vision and Pattern Recognition (CVPR)*.
- Binbin Huang, Zehao Yu, Anpei Chen, Andreas Geiger, and Shenghua Gao. 2024. 2d gaussian splatting for geometrically accurate radiance fields. In *ACM SIGGRAPH 2024 Conference Papers*. 1–11.
- Changwon Jang, Kiseung Bang, Minseok Chae, Byoungcho Lee, and Douglas Lanman. 2024. Waveguide holography for 3D augmented reality glasses. *Nature Communications* 15, 1 (2024), 66.
- Bahram Javid, Artur Carnicer, Arun Anand, George Barbastathis, Wen Chen, Pietro Ferraro, JW Goodman, Ryoichi Horisaki, Kedar Khare, Malgorzata Kujawinska, et al. 2021. Roadmap on digital holography. *Optics Express* 29, 22 (2021), 35078–35118.
- James T Kajiya and Brian P Von Herzen. 1984. Ray tracing volume densities. *ACM SIGGRAPH computer graphics* 18, 3 (1984), 165–174.
- Hoonjong Kang, Takeshi Yamaguchi, and Hiroshi Yoshikawa. 2008. Accurate phase-added stereogram to improve the coherent stereogram. *Applied optics* 47, 19 (2008), D44–D54.
- Bernhard Kerbl, Georgios Kopanas, Thomas Leimkühler, and George Drettakis. 2023. 3D Gaussian Splatting for Real-Time Radiance Field Rendering. *ACM TOG* 42, 4 (July 2023).
- Shakiba Kheradmand, Daniel Rebin, Gopal Sharma, Weiwei Sun, Yang-Che Tseng, Hossain Isack, Abhishek Kar, Andrea Tagliasacchi, and Kwang Moo Yi. 2024. 3D Gaussian Splatting as Markov Chain Monte Carlo. In *NeurIPS*.
- Dongyeon Kim, Seung-Woo Nam, Suyeon Choi, Jong-Mo Seo, Gordon Wetzstein, and Yoonchan Jeong. 2024a. Holographic parallax improves 3D perceptual realism. *ACM Transactions on Graphics (TOG)* 43, 4 (2024), 1–13.
- Dongyeon Kim, Seung-Woo Nam, Suyeon Choi, Jong-Mo Seo, Gordon Wetzstein, and Yoonchan Jeong. 2024b. Holographic Parallax Improves 3D Perceptual Realism. *ACM Transactions on Graphics (TOG)* 43, 4, Article 68 (2024), 13 pages.
- Dongyeon Kim, Seung-Woo Nam, Byoungcho Lee, Jong-Mo Seo, and Byoungcho Lee. 2022b. Accommodative holography: improving accommodation response for perceptually realistic holographic displays. *ACM Trans. Graph.* 41, 4, Article 111 (July 2022), 15 pages. <https://doi.org/10.1145/3528223.3530147>
- Jonghyun Kim, Manu Gopakumar, Suyeon Choi, Yifan Peng, Ward Lopes, and Gordon Wetzstein. 2022a. Holographic Glasses for Virtual Reality. In *ACM SIGGRAPH 2022 Conference Proceedings* (Vancouver, BC, Canada) (SIGGRAPH ’22). Association for Computing Machinery, New York, NY, USA, Article 33, 9 pages. <https://doi.org/10.1145/3528233.3530739>
- Grace Kuo, Florian Schiffers, Douglas Lanman, Oliver Cossairt, and Nathan Matsuda. 2023. Multisource holography. *ACM Transactions on Graphics (TOG)* 42, 6 (2023), 1–14.
- Byoungcho Lee, Dongyeon Kim, Seungjae Lee, Chun Chen, and Byoungcho Lee. 2022. High-contrast, speckle-free, true 3D holography via binary CGH optimization. *Scientific Reports* 12, 1 (2022), 2811. <https://doi.org/10.1038/s41598-022-06405-2>
- Seungjae Lee, Dongyeon Kim, Seung-Woo Nam, Byoungcho Lee, Jaebum Cho, and Byoungcho Lee. 2020. Light source optimization for partially coherent holographic displays with consideration of speckle contrast, resolution, and depth of field. *Scientific reports* 10, 1 (2020), 18832.
- Mark E Lucente. 1993. Interactive computation of holograms using a look-up table. *Journal of Electronic Imaging* 2, 1 (1993), 28–34.
- Andrew Maimone, Andreas Georgiou, and Joel S Kollin. 2017. Holographic near-eye displays for virtual and augmented reality. *ACM Transactions on Graphics (TOG)* 36, 4 (2017), 1–16.
- Kyoji Matsushima. 2005a. Computer-generated holograms for three-dimensional surface objects with shade and texture. *Applied optics* 44, 22 (2005), 4607–4614.
- Kyoji Matsushima. 2005b. Exact hidden-surface removal in digitally synthetic full-parallax holograms. In *Practical Holography XIX: Materials and Applications*, Vol. 5742. SPIE, 25–32.
- Kyoji Matsushima. 2020. *Introduction to Computer Holography: Creating Computer-Generated Holograms as the Ultimate 3D Image*. Springer Nature.
- Kyoji Matsushima and Sumio Nakahara. 2009. Extremely high-definition full-parallax computer-generated hologram created by the polygon-based method. *Applied optics* 48, 34 (2009), H54–H63.
- Kyoji Matsushima, Masaki Nakamura, and Sumio Nakahara. 2014. Silhouette method for hidden surface removal in computer holography and its acceleration using the switch-back technique. *Optics express* 22, 20 (2014), 24450–24465.
- Kyoji Matsushima, Hagen Schimmel, and Frank Wyrowski. 2003. Fast calculation method for optical diffraction on tilted planes by use of the angular spectrum of plane waves. *JOSA A* 20, 9 (2003), 1755–1762.
- Kyoji Matsushima and Tomoyoshi Shimobaba. 2009. Band-limited angular spectrum method for numerical simulation of free-space propagation in far and near fields. *Optics express* 17, 22 (2009), 19662–19673.
- Kyoji Matsushima and Noriaki Sonobe. 2018. Full-color digitized holography for large-scale holographic 3D imaging of physical and nonphysical objects. *Applied Optics* 57, 1 (2018), A150–A156.
- Olivier Mercier, Yusuf Sulai, Kevin J MacKenzie, Marina Zannoli, James Hillis, Derek Nowrouzezahrai, and Douglas Lanman. 2017. Fast gaze-contingent optimal decompositions for multifocal displays. *ACM Trans. Graph.* 36, 6 (2017), 237–1.
- Ben Mildenhall, Pratul P. Srinivasan, Matthew Tancik, Jonathan T. Barron, Ravi Ramamoorthi, and Ren Ng. 2020. NeRF: Representing Scenes as Neural Radiance Fields for View Synthesis. In *ECCV*.

- Rahul Narain, Rachel A. Albert, Abdullah Bulbul, Gregory J. Ward, Martin S. Banks, and James F. O'Brien. 2015. Optimal presentation of imagery with focus cues on multi-plane displays. *ACM Trans. Graph.* 34, 4, Article 59 (July 2015), 12 pages. <https://doi.org/10.1145/2766909>
- Nitish Padmanaban, Yifan Peng, and Gordon Wetzstein. 2019. Holographic near-eye displays based on overlap-add stereograms. *ACM Transactions on Graphics (TOG)* 38, 6 (2019), 1–13.
- Jae-Hyeung Park. 2017. Recent progress in computer-generated holography for three-dimensional scenes. *Journal of Information Display* 18, 1 (2017), 1–12.
- Jae-Hyeung Park and Mehdi Askari. 2019. Non-hogel-based computer generated hologram from light field using complex field recovery technique from Wigner distribution function. *Optics express* 27, 3 (2019), 2562–2574.
- Pierre Pellat-Finet. 1994. Fresnel diffraction and the fractional-order Fourier transform. *Optics Letters* 19, 18 (1994), 1388–1390.
- Yifan Peng, Suyeon Choi, Jonghyun Kim, and Gordon Wetzstein. 2021. Speckle-free holography with partially coherent light sources and camera-in-the-loop calibration. *Science advances* 7, 46 (2021), eabg5040.
- Yifan Peng, Suyeon Choi, Nitish Padmanaban, and Gordon Wetzstein. 2020. Neural holography with camera-in-the-loop training. *ACM Transactions on Graphics (TOG)* 39, 6 (2020), 1–14.
- Dapu Pi, Juan Liu, and Yongtian Wang. 2022. Review of computer-generated hologram algorithms for color dynamic holographic three-dimensional display. *Light: Science & Applications* 11, 1 (2022), 231.
- Thomas Porter and Tom Duff. 1984. Compositing digital images. *SIGGRAPH Comput. Graph.* 18, 3 (Jan. 1984), 253–259. <https://doi.org/10.1145/964965.808606>
- Yijun Qi, Chenliang Chang, and Jun Xia. 2016. Speckleless holographic display by complex modulation based on double-phase method. *Optics express* 24, 26 (2016), 30368–30378.
- Florian Schiffrers, Praneeth Chakravarthula, Nathan Matsuda, Grace Kuo, Ethan Tseng, Douglas Lanman, Felix Heide, and Oliver Cossairt. 2023. Stochastic light field holography. In *2023 IEEE International Conference on Computational Photography (ICCP)*. IEEE, 1–12.
- Kaifeng Sheng, Zheng Zhou, Yingliang Peng, and Qianwei Wang. 2025. 2D Triangle Splatting for Direct Differentiable Mesh Training. arXiv:2506.18575 [cs.CV] <https://arxiv.org/abs/2506.18575>
- Liang Shi, Beichen Li, Changil Kim, Petr Kellnhofer, and Wojciech Matusik. 2021. Towards real-time photorealistic 3D holography with deep neural networks. *Nature* 591, 7849 (2021), 234–239.
- Liang Shi, Beichen Li, and Wojciech Matusik. 2022. End-to-end learning of 3d phase-only holograms for holographic display. *Light: Science & Applications* 11, 1 (2022), 247.
- Liang Shi, DongHun Ryu, and Wojciech Matusik. 2024. Ergonomic-Centric Holography: Optimizing Realism, Immersion, and Comfort for Holographic Display. *Laser & Photonics Reviews* n/a, n/a (2024), 2300651. <https://doi.org/10.1002/lpor.202300651>
- Tomoyoshi Shimobaba and Tomoyoshi Ito. 2015. Random phase-free computer-generated hologram. *Optics express* 23, 7 (2015), 9549–9554.
- Pierre St-Hilaire. 1995. Phase profiles for holographic stereograms. *Optical Engineering* 34, 1 (1995), 83–89.
- Jiaxiang Tang, Hang Zhou, Xiaokang Chen, Tianshu Hu, Errui Ding, Jingdong Wang, and Gang Zeng. 2023. Delicate Textured Mesh Recovery from NeRF via Adaptive Surface Refinement. In *ICCV*.
- Peter Wai Ming Tsang and T-C Poon. 2013. Novel method for converting digital Fresnel hologram to phase-only hologram based on bidirectional error diffusion. *Optics express* 21, 20 (2013), 23680–23686.
- Fahri Yaraş, Hoonjong Kang, and Levent Onural. 2010. State of the art in holographic displays: a survey. *Journal of display technology* 6, 10 (2010), 443–454.
- Vickie Ye, Ruilong Li, Justin Kerr, Matias Turkulainen, Brent Yi, Zhuoyang Pan, Otto Seiskari, Jianbo Ye, Jeffrey Hu, Matthew Tancik, and Angjoo Kanazawa. 2024. gsplat: An Open-Source Library for Gaussian Splatting. *arXiv preprint arXiv:2409.06765* (2024). arXiv:2409.06765 [cs.CV] <https://arxiv.org/abs/2409.06765>
- Dongheon Yoo, Youngjin Jo, Seung-Woo Nam, Chun Chen, and Byoungheon Lee. 2021. Optimization of computer-generated holograms featuring phase randomness control. *Optics Letters* 46, 19 (2021), 4769–4772.
- Hao Zhang, Liangcai Cao, and Guofan Jin. 2019. Three-dimensional computer-generated hologram with Fourier domain segmentation. *Optics express* 27, 8 (2019), 11689–11697.
- Jingzhao Zhang, Nicolas Pégard, Jingshan Zhong, Hillel Adesnik, and Laura Waller. 2017. 3D computer-generated holography by non-convex optimization. *Optica* 4, 10 (2017), 1306–1313.

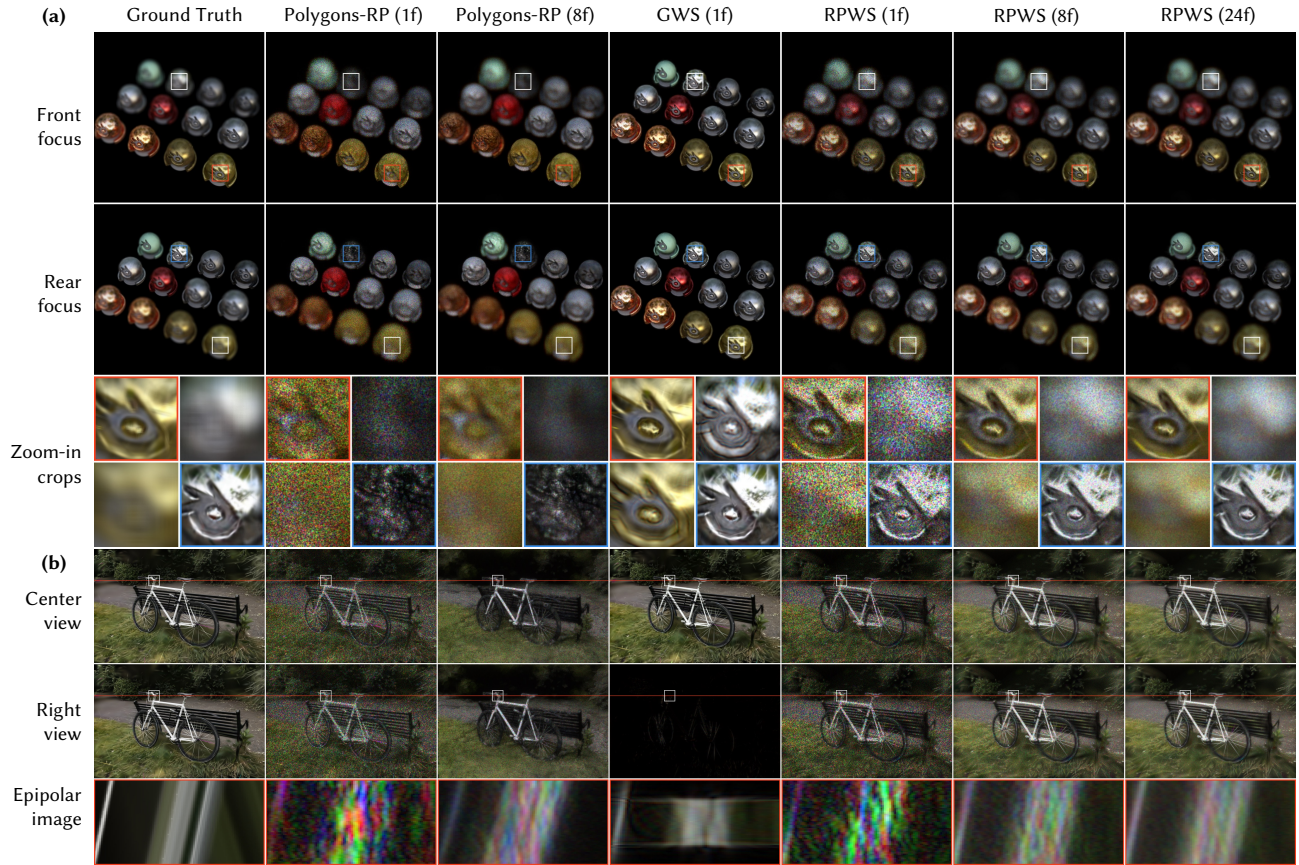


Fig. 4. **Simulated 3D focal stacks and 4D light fields reconstructed from various baseline CGH algorithms.** The image quality of random-phase polygons-based CGH (Polygons-RP) is inherently limited by the coarse per-face textured mesh representation, resulting in poor image quality even in in-focus regions. GWS [Choi et al. 2025a] reconstructs sharp details at in-focus regions, but suffers from large depth of field and unnatural ringing artifacts. Our method (RPWS) generates sharp content at focused regions and the resulting hologram has shallow depth of field, reconstructing natural defocus blur across different depths. With additional time-multiplexing, the image quality of RPWS significantly improves.

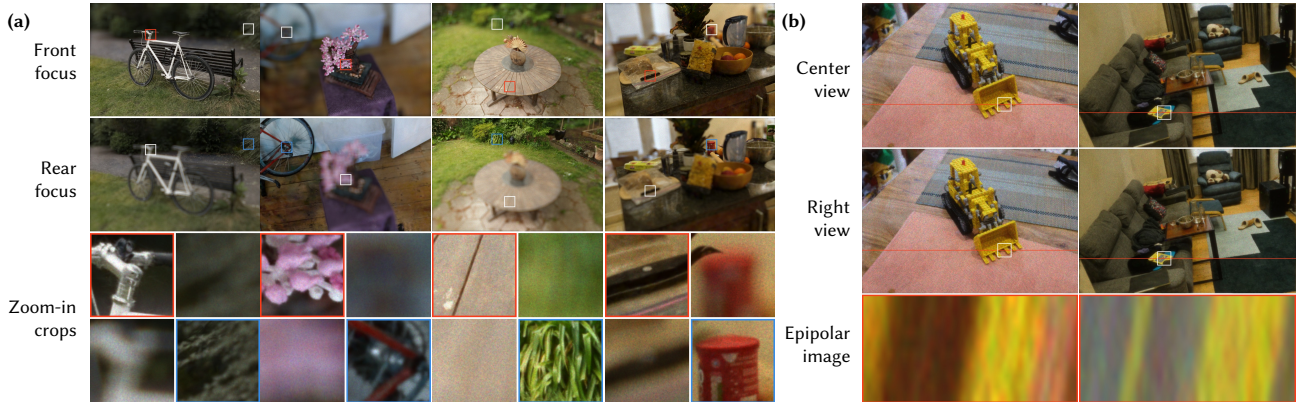


Fig. 5. **Simulated 3D focal stacks and 4D light fields reconstructed from RPWS of triangle splats [Held et al. 2025a].** We run our RPWS algorithm on Triangle splats proposed by Held et al. [2025a]. RPWS with triangle splats accurately reconstructs natural defocus blur and parallax on a wide variety of scenes, validating the robustness of our method to different translucent primitive types.

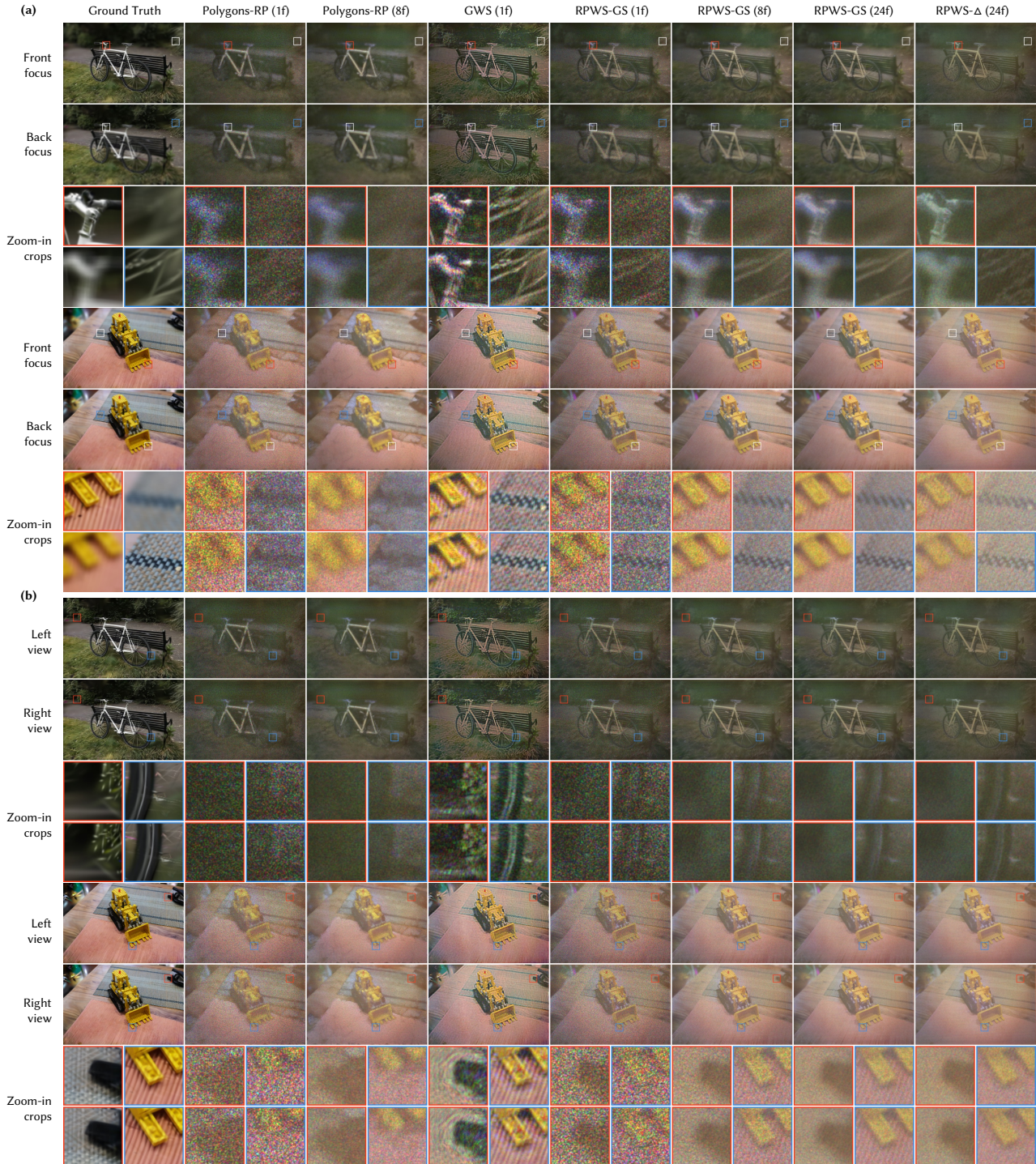


Fig. 6. **Experimentally captured 3D focal stacks and 4D light fields of holograms generated using different CGH algorithms.** Polygon-based CGH (Polygons-RP) [Matsushima 2005a; Matsushima and Nakahara 2009; Matsushima et al. 2014] achieves low image quality due to the low quality of the underlying textured mesh 3D representation. GWS [Choi et al. 2025a] generates smooth-phase holograms, resulting in limited defocus blur with unnatural ringing artifacts and little-to-no parallax. Our method, RPWS with Gaussian (–GS) and triangle splatting (– Δ) variants, achieves good image quality in in-focus regions, reconstructs natural incoherent blur in defocus regions, and shows significantly more parallax than GWS. With 24 frames time-multiplexing, RPWS (both –GS and – Δ variants) achieves near speckle-free results.